Electronic Supplementary Material (ESI) for Dalton Transactions.

SUPPORTING INFORMATION

Mechanochemical Synthesis of Crystalline and Amorphous Digold(I) Helicates Exhibiting Anion- and Phase-Switchable Luminescent Properties

Csaba Jobbágy,[a] Miklós Molnár,[a] Péter Baranyai[b] and Andrea Deák*[a]

[a] Hungarian Academy of Sciences, MTA TTK SZKI Lendület Supramolecular Chemistry Laboratory and
[b] Hungarian Academy of Sciences, MTA TTK AKI
H-1117 Budapest, Magyar Tudósok körútja 2,
Hungary

General Procedures and Physical Measurements

All chemicals and solvents used for the syntheses were of reagent grade. The solvents for synthesis were used without further purification. All manipulations were performed in air. $[Au_2L_2](NO_3)_2$ was prepared according to a published procedure.[1] Mechanochemical reactions were performed by a Retsch MM400 shaker mill in a 5 mL agate jar with two 7 mm diameter agate balls operating at 25 Hz. The elemental analysis has been carried out with an Elementar Vario EL III apparatus. Infrared spectra were recorded in the 400 to 4000 cm^{-1} spectral range on a Varian 2000 FT-IR spectrometer equipped with Golden Gate single reflection diamond ATR (Specac Ltd.). Optical micrographs were recorded with a Nikon Eclipse LV100 microscope equipped with Nikon DS-Fi2 digital camera (Auro-Science Consulting Kft., Budapest, Hungary). Steady state and time-resolved luminescence measurements were carried out on an Edinburgh Instrument FLSP920 spectrofluorimeter. Spectral corrections were applied using excitation and emission correction functions of the instrument. The solid-state room temperature emission studies were conducted on finely ground powder samples placed on a Quartz Suprasil plate in a front face sample holder. Longpass filters were used to exclude the scattered excitation light. The excitation light source was a μF900H xenon flashlamp (pulse duration: 2 μs at FWHM) for the luminescent lifetime measurements. Powder diffractograms were produced with Cu-K_α radiation on a vertical high-angle Philips PW 1050 powder diffractometer.

Dichloromethane-assisted mechanochemical synthesis of *crystalline c*-$[Au_2L_2](X)_2$ and water-assisted mechanochemical synthesis of *amorphous a*-$[Au_2L_2](X)_2$ (X = CF_3SO_3, SCN, BF_4 and PF_6) digold(I) helicates

The mechanochemical anion-exchange reactions were performed by ball-milling compound $[Au_2L_2](NO_3)_2$ (335 mg, 0.2 mmol) with NaX salts in a 1:2 (X = CF_3SO_3, SCN, BF_4 and PF_6) molar ratio with Retsch MM400 shaker mill in a 5 mL agate jar with two 7 mm diameter agate balls with 120 μL dichloromethane or 80 μL of water, respectively. The mixture was then ground for 5 minutes at 25 Hz. The mechanochemical reactions produce a powder mixture containing anion-exchanged products $[Au_2L_2](X)_2$ and $NaNO_3$, which after thorough washing with water provided pure anion-exchanged $[Au_2L_2](X)_2$ helicates. The dichloromethane assisted grinding reactions lead to *crystalline c*-$[Au_2L_2](X)_2$ compounds, in contrast to water assisted grinding that provided *amorphous a*-$[Au_2L_2](X)_2$ products.

Optical microscopic graphs of these anion-exchanged *crystalline* *c*-$[Au_2L_2](X)_2$ and *amorphous* *a*-$[Au_2L_2](X)_2$ (X = CF_3SO_3, SCN, BF_4 and PF_6) products are shown in Figures S1 and S2, respectively. FT-IR spectra, emission (λ_{ex} = 365 nm) and excitation spectra and the PXRD patterns of crystalline *c*-$[Au_2L_2](X)_2$ and amorphous *a*-$[Au_2L_2](X)_2$ complexes (X = CF_3SO_3, SCN, BF_4 and PF_6) are given in Fig.S3–S18. Emission, excitation characteristics and lifetimes of crystalline *c*-$[Au_2L_2](X)_2$ and amorphous *a*-$[Au_2L_2](X)_2$ complexes (X = CF_3SO_3, SCN, BF_4 and PF_6) are listed in Table S1.

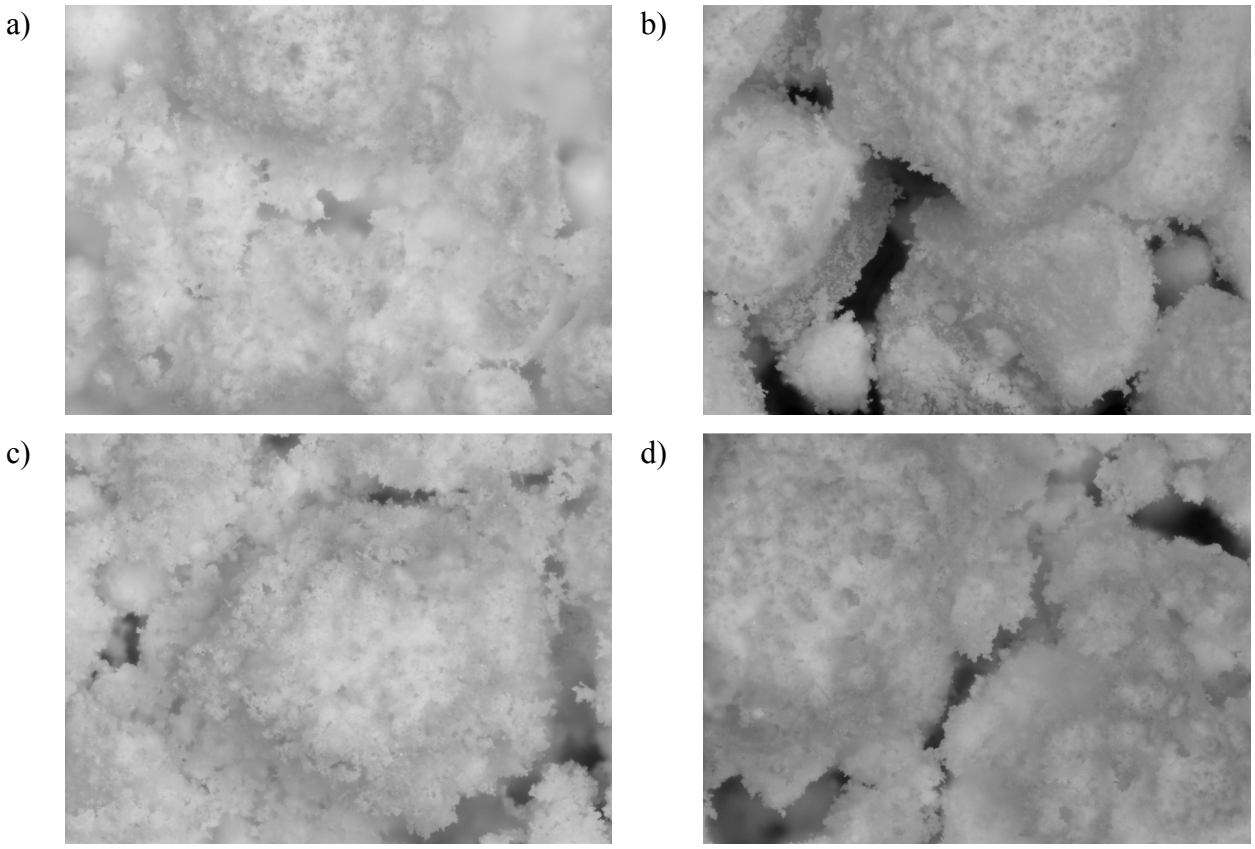

Fig. S1 Optical microscopic graphs of *crystalline* a) *c*-$[Au_2L_2](CF_3SO_3)_2$, b) *c*-$[Au_2L_2](SCN)_2$, c) *c*-$[Au_2L_2](BF_4)_2$ and d) *c*-$[Au_2L_2](PF_6)_2$ helicates obtained from dichloromethane-assisted grinding reactions.

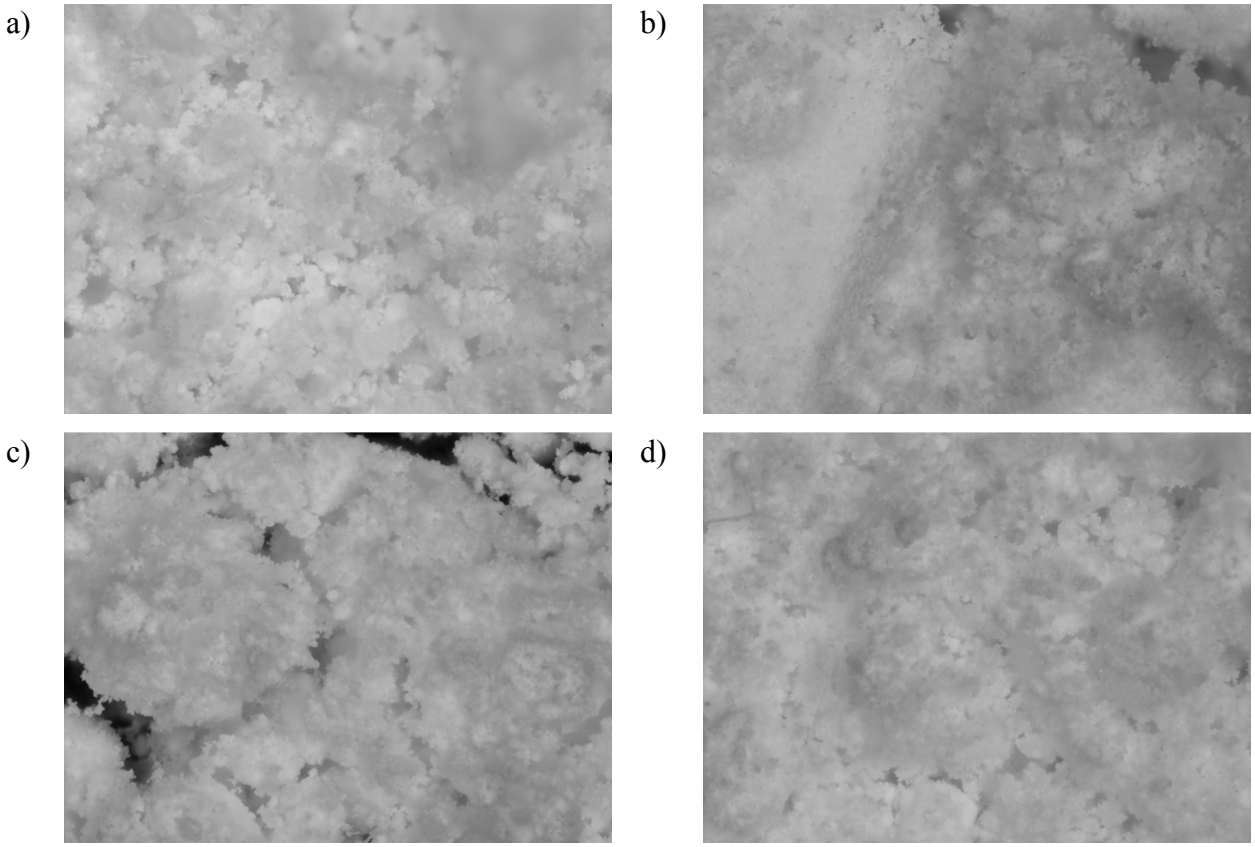

Fig. S2 Optical microscopic graphs of *amorphous* a) *a*-$[Au_2L_2](CF_3SO_3)_2$, b) *a*-$[Au_2L_2](SCN)_2$, c) *a*-$[Au_2L_2](BF_4)_2$ and d) *a*-$[Au_2L_2](PF_6)_2$ helicates obtained from water-assisted grinding reactions.

Crystalline *c*-[Au_2L_2](CF_3SO_3)$_2$

IR data: 3078 (w), 2967 (w), 1607 (w), 1584 (w), 1480 (w), 1437 (m), 1404 (s), 1257 (s), 1222 (s),1147 (s), 1096 (m), 1029 (s), 999 (m), 874 (w), 742 (m), 688 (m), 635 (m); Elemental analysis calcd. (%) for *c*-[Au_2L_2](CF_3SO_3)$_2$: C 51.96, H 3.49; found: C 51.48, H 3.53.

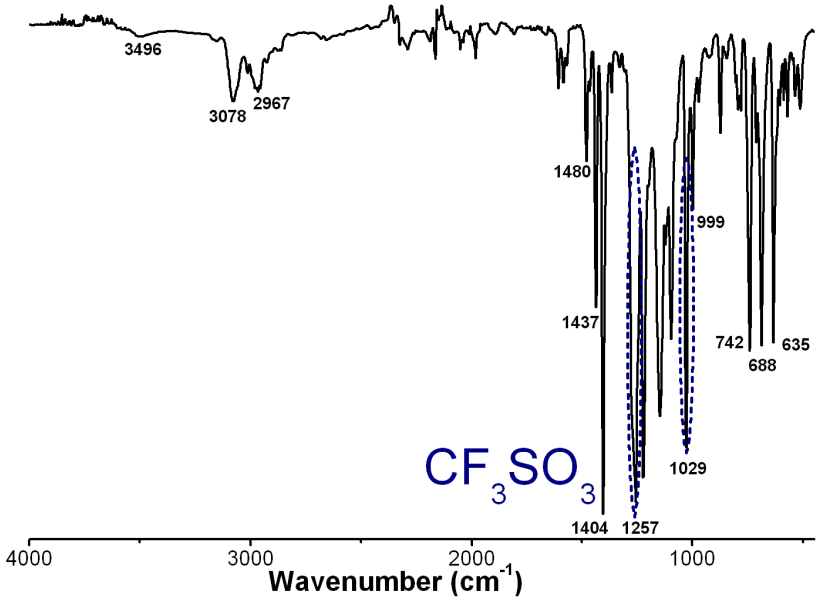

Fig. S3 FT-IR spectra of crystalline *c*-[Au_2L_2](CF_3SO_3)$_2$ complex.

Amorphous *a*-[Au_2L_2](CF_3SO_3)$_2$

IR data: 3492 (b, w), 3075 (w), 2978 (w), 1609 (w), 1586 (w), 1481 (w), 1437 (m), 1403 (s), 1259 (s), 1221 (s), 1149 (s), 1097 (m), 1029 (s), 999 (m), 873 (w), 742 (m), 689 (m), 635 (m); Elemental analysis calcd. (%) for *a*-[Au_2L_2](CF_3SO_3)$_2$·1.5 H_2O: C 51.21, H 3.60; found: C 51.30, H 3.76.

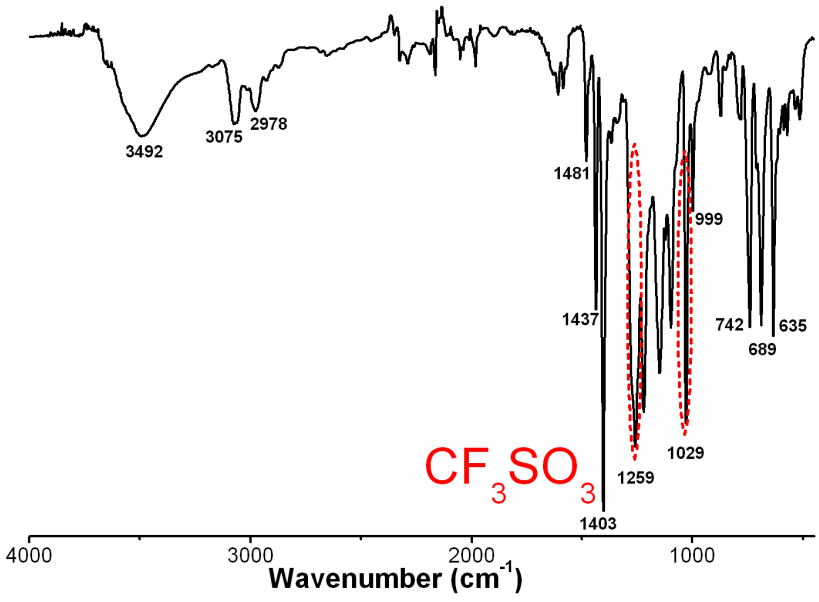

Fig. S4 FT-IR spectra of amorphous *a*-[Au_2L_2](CF_3SO_3)$_2$ complex.

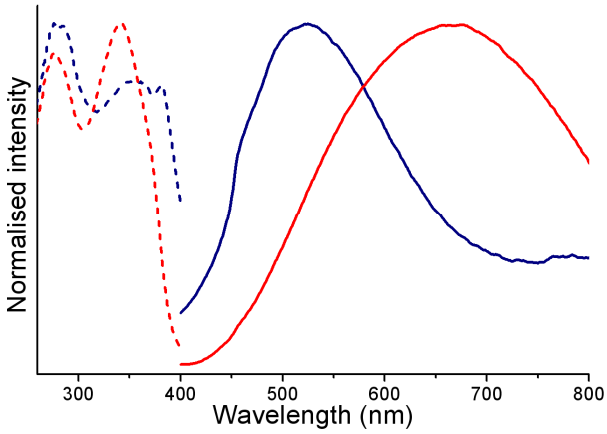

Fig. S5 Emission (solid lines) and excitation (dashed lines) spectra of crystalline *c*-$[Au_2L_2](CF_3SO_3)_2$ (blue coloured) and amorphous *a*-$[Au_2L_2](CF_3SO_3)_2$ (red coloured) helicates.

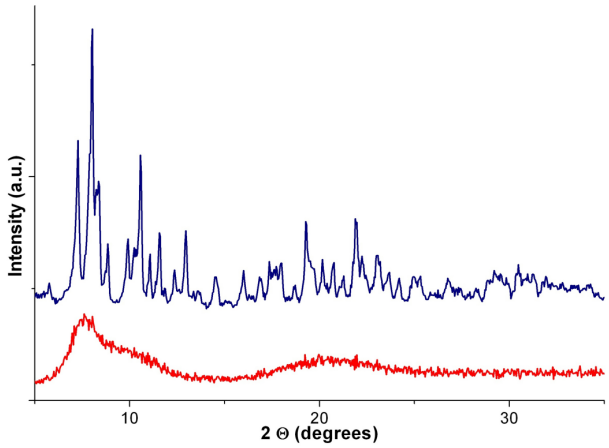

Fig. S6 PXRD patterns of crystalline *c*-$[Au_2L_2](CF_3SO_3)_2$ (blue coloured) and amorphous *a*-$[Au_2L_2](CF_3SO_3)_2$ (red coloured) complexes.

Crystalline *c*-[Au_2L_2](SCN)$_2$

IR data: 3445 (vw), 3057 (w), 2970 (w), 2108 (s), 1480 (w), 1434 (m), 1404 (s), 1230 (m), 1097 (m), 999 (w), 737 (m), 687 (m); Elemental analysis calcd. (%) for *c*-[Au_2L_2](SCN)$_2$: C 57.63, H 3.87, N 1.68; found: C 57.98, H 3.92, N 1.71.

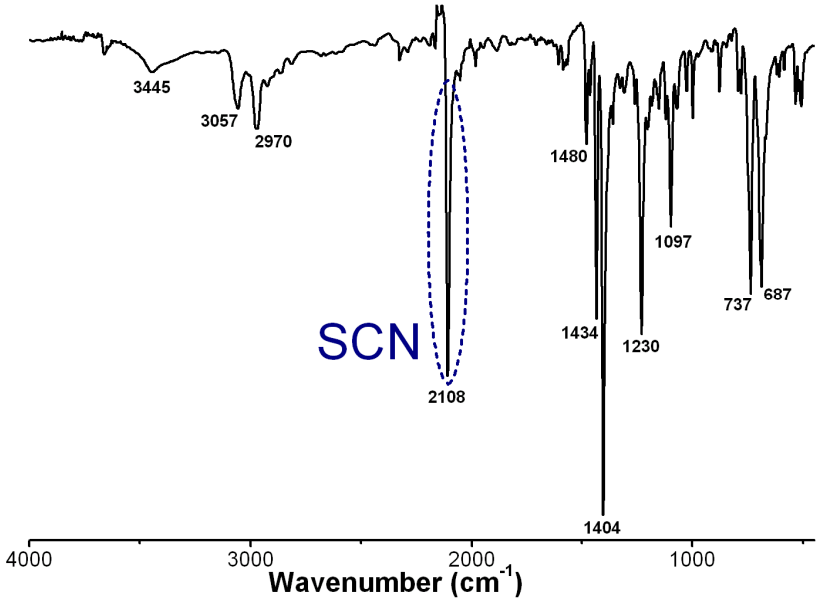

Fig. S7 FT-IR spectra of crystalline *c*-[Au_2L_2](SCN)$_2$ complex.

Amorphous *a*-[Au_2L_2](SCN)$_2$

IR data: 3408 (b, w), 3056 (w), 2974 (w), 2099 (s), 2052 (w), 1607 (w), 1586 (w), 1480 (w), 1435 (m), 1402 (s), 1222 (m), 1097 (m), 741 (m), 689 (m); Elemental analysis calcd. (%) for *a*-[Au_2L_2](SCN)$_2$·3 H_2O: C 55.82, H 4.10, N 1.63; found: C 55.82, H 4.08, N 1.49.

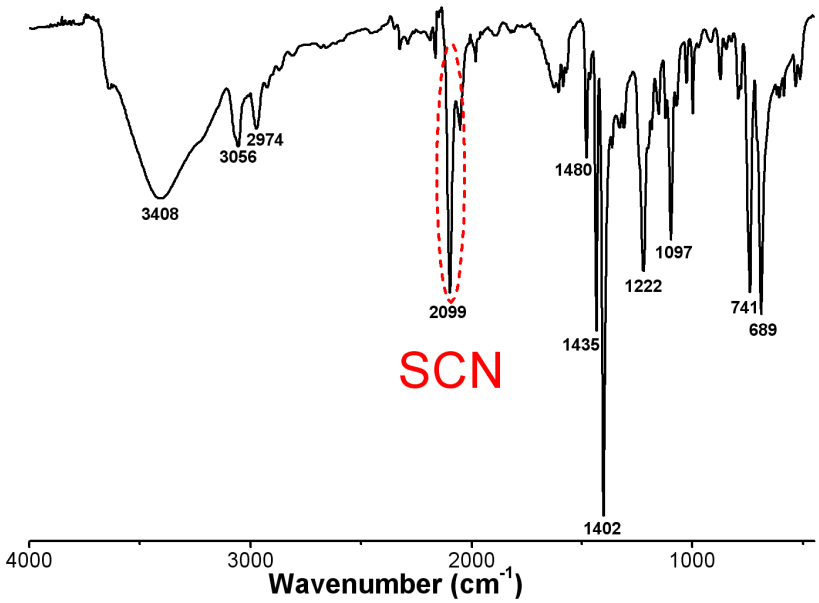

Fig. S8 FT-IR spectra of amorphous *a*-[Au_2L_2](SCN)$_2$ complex.

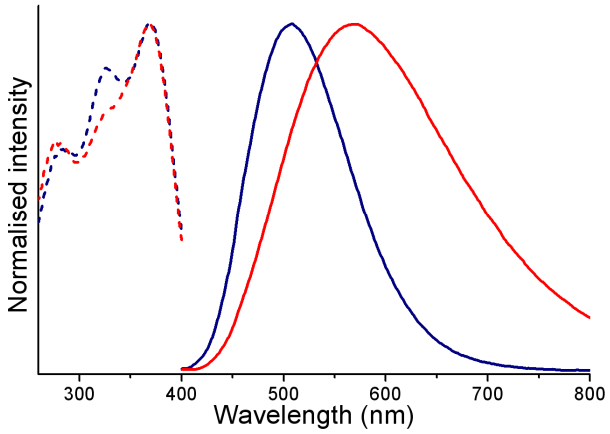

Fig. S9 Emission (solid lines) and excitation (dashed lines) spectra of crystalline *c*-$[Au_2L_2](SCN)_2$ (blue coloured) and amorphous *a*-$[Au_2L_2](SCN)_2$ (red coloured) helicates.

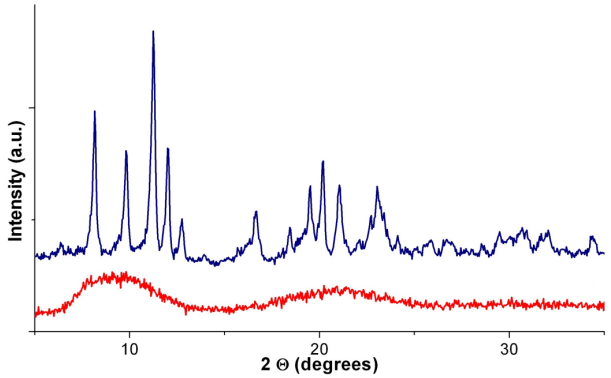

Fig. S10 PXRD patterns of crystalline *c*-$[Au_2L_2](SCN)_2$ (blue coloured) and amorphous *a*-$[Au_2L_2](SCN)_2$ (red coloured) complexes.

Crystalline *c*-[Au_2L_2](BF_4)$_2$

IR data: 3645 (w), 3077 (w), 2975 (w), 2165 (w), 1607 (w), 1586 (w), 1480 (w), 1436 (m), 1402 (s), 1216 (m), 1097 (m), 1057 (m), 1036 (m), 998 (m), 870 (w), 744 (m), 688 (m); Elemental analysis calcd. (%) for *c*-[Au_2L_2](BF_4)$_2$·0.5 H_2O: C 54.03, H 3.78; found: C 53.98, H 3.90.

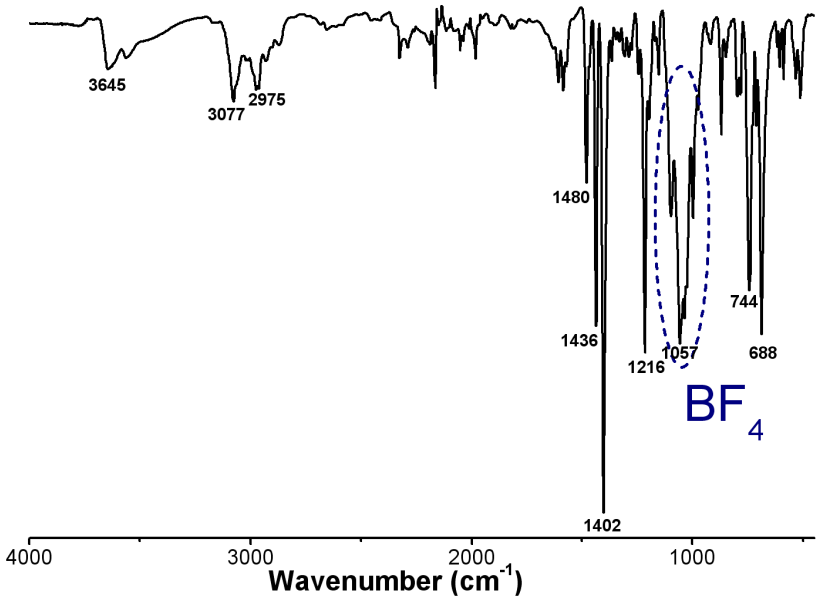

Fig. S11 FT-IR spectra of crystalline *c*-[Au_2L_2](BF_4)$_2$ complex.

Amorphous *a*-[Au_2L_2](BF_4)$_2$

IR data: 3626 (b, w), 3061 (w), 2976 (w), 2165 (w), 1608 (w), 1585 (w), 1480 (w), 1436 (m), 1402 (s), 1219 (m), 1052 (s), 997 (m), 872 (w), 742 (m), 689 (m); Elemental analysis calcd. (%) for *a*-[Au_2L_2](BF_4)$_2$·1.5 H_2O: C 53.48, H 3.86; found: C 53.66, H 3.90.

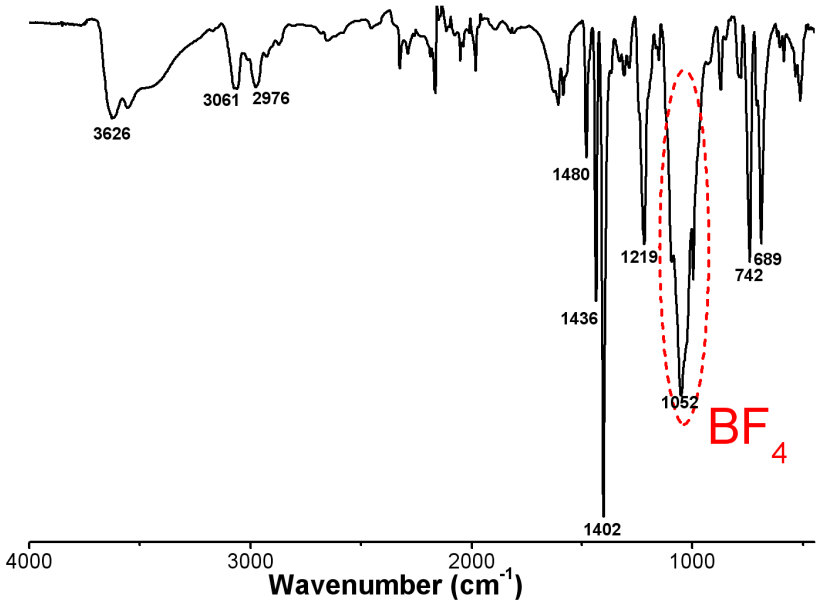

Fig. S12 FT-IR spectra of amorphous *a*-[Au_2L_2](BF_4)$_2$ complex.

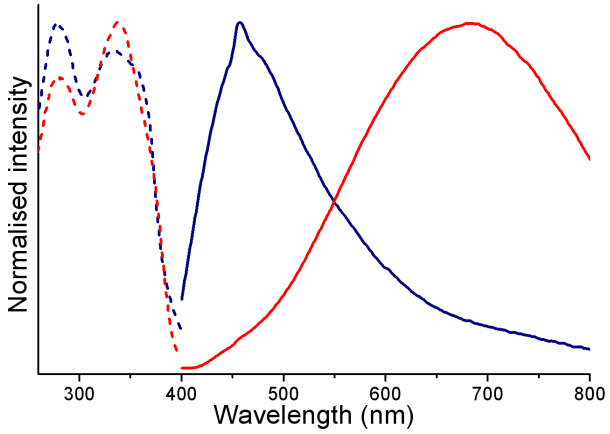

Fig. S13 Emission (solid lines) and excitation (dashed lines) spectra of crystalline *c*-$[Au_2L_2](BF_4)_2$ (blue coloured) and amorphous *a*-$[Au_2L_2](BF_4)_2$ (red coloured) helicates.

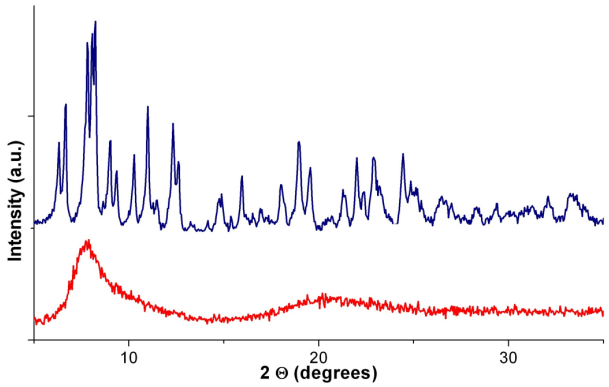

Fig. S14 PXRD patterns of crystalline *c*-$[Au_2L_2](BF_4)_2$ (blue coloured) and amorphous *a*-$[Au_2L_2](BF_4)_2$ (red coloured) complexes.

Crystalline *c*-[Au_2L_2](PF_6)$_2$

IR data: 3653 (w), 3409 (b, w), 3076 (w), 2981 (w), 1609 (w), 1481 (w), 1437 (m), 1403 (s), 1218 (m), 1099 (m), 999 (w), 829 (s), 787 (m), 740 (m), 711 (m), 688 (m), 556 (m); Elemental analysis calcd. (%) for *c*-[Au_2L_2](PF_6)$_2$·1.5 H_2O: C 50.15, H 3.61; found: C 50.11, H 3.61.

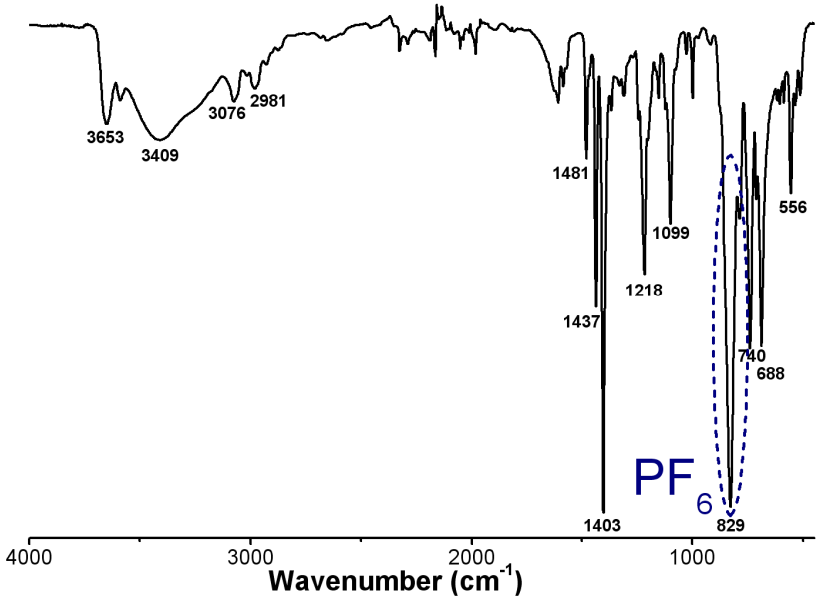

Fig. S15 FT-IR spectra of crystalline *c*-[Au_2L_2](PF_6)$_2$ complex.

Amorphous *a*-[Au_2L_2](PF_6)$_2$

IR data: 3660 (w), 3433 (vw), 3074 (w), 2978 (w), 1609 (w), 1586 (w), 1481 (w), 1437 (m), 1403 (s), 1219 (m), 1098 (m), 1000 (w), 831 (s), 786 (m), 740 (m), 688 (m), 556 (m) 513 (w); Elemental analysis calcd. (%) for *a*-[Au_2L_2](PF_6)$_2$: C 50.88, H 3.50; found: C 50.91, H 3.77.

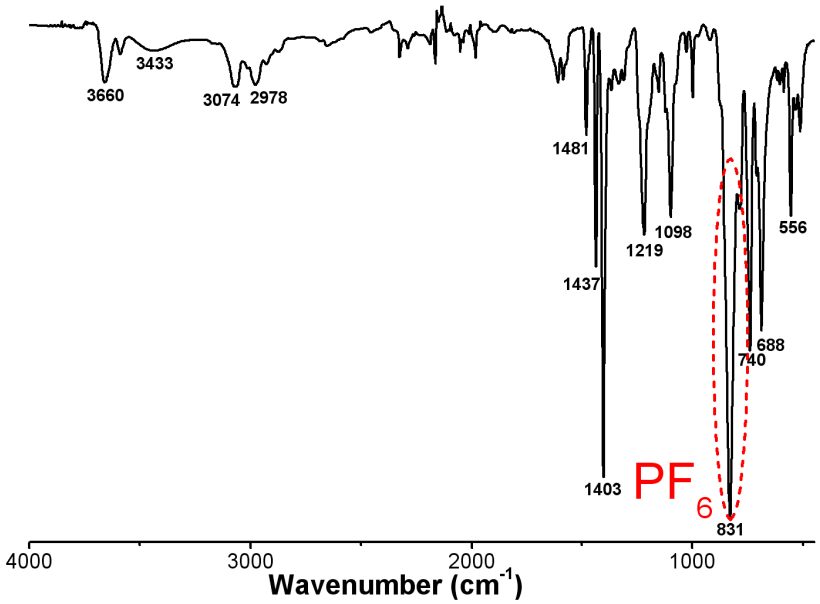

Fig. S16 FT-IR spectra of amorphous *a*-[Au_2L_2](PF_6)$_2$ complex.

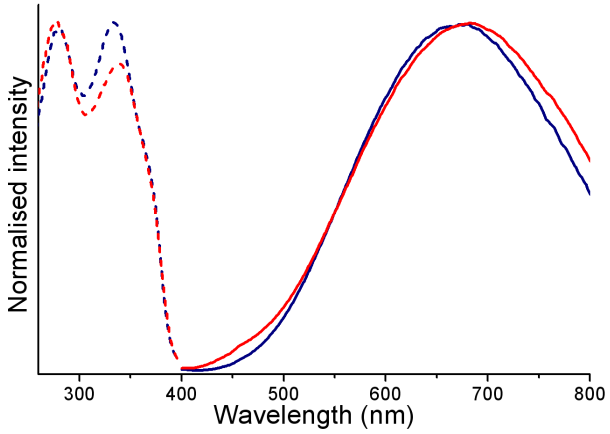

Fig. S17 Emission (solid lines) and excitation (dashed lines) spectra of crystalline *c*-$[Au_2L_2](PF_6)_2$ (blue coloured) and amorphous *a*-$[Au_2L_2](PF_6)_2$ (red coloured) helicates.

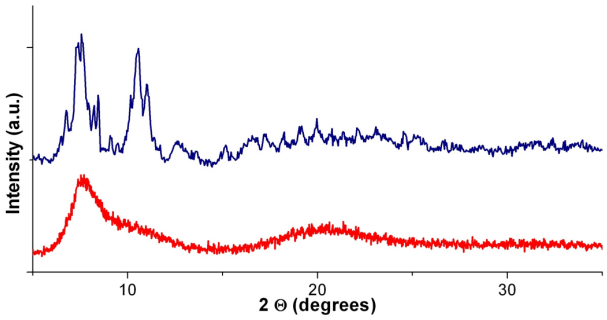

Fig. S18 PXRD patterns of crystalline *c*-$[Au_2L_2](PF_6)_2$ (blue coloured) and amorphous *a*-$[Au_2L_2](PF_6)_2$ (red coloured) complexes.

Table S1 Emission, excitation characteristics and lifetimes of crystalline *c*-$[Au_2L_2](X)_2$ and amorphous *a*-$[Au_2L_2](X)_2$ (X = CF_3SO_3, SCN, BF_4 and PF_6) helicates.

Compound	λ_{em} (nm)	λ_{ex} (nm)	τ_1 (μs)	τ_2 (μs)
c-$[Au_2L_2](CF_3SO_3)_2$	460 sh, 525	280, 355, 381	2.5 (73%)	15 (27%)
a-$[Au_2L_2](CF_3SO_3)_2$	670	277, 340	3.1 (34%)	14 (66%)
c-$[Au_2L_2](SCN)_2$	508	285, 326, 368	0.3 (52%)	5.9 (48%)
a-$[Au_2L_2](SCN)_2$	570	279, 322 sh, 368	1.2 (46%)	8.9 (54%)
c-$[Au_2L_2](BF_4)_2$	447 sh, 457, 482 sh	279, 334, 355 sh	3.8 (34%)	16 (66%)
a-$[Au_2L_2](BF_4)_2$	685	280, 338	3.9 (35%)	14 (65%)
c-$[Au_2L_2](PF_6)_2$	675	279, 333	2.7 (32%)	13 (68%)
a-$[Au_2L_2](PF_6)_2$	682	276, 338	4.5 (37%)	15 (63%)

General procedure for reversible crystalline-to-amorphous (CTA) and amorphous-to-crystalline (ATC) transformations achieved by solvent-assisted ball-milling

Reversible CTA/ATC transformations were performed using 0.05 mmol of crystalline or amorphous $[Au_2L_2](X)_2$ (X = CF_3SO_3 and BF_4) samples placed into 5 mL agate jar with two 7 mm diameter agate balls. 20 μL of water (for CTA transformation) or 30 μL dichloromethane (for ATC transformation) was added into the jar and the sample was ground with a Retsch MM400 shaker mill operating at 25 Hz for the specified time. The crystalline *c*-$[Au_2L_2](CF_3SO_3)_2$ and *c*-$[Au_2L_2](BF_4)_2$ helicates were amorphized by mechanical milling (CTA phase transformation) after 10 and 60 minutes, respectively. After 2 and 3 minutes of ball-milling with dichloromethane, these amorphous *a*-$[Au_2L_2](CF_3SO_3)_2$ and *a*-$[Au_2L_2](BF_4)_2$ materials were converted back into their crystalline counterparts (ATC transformation).

The emission spectra (λ_{ex} = 365 nm) of amorphous *a*-$[Au_2L_2](X)_2$ (X = CF_3SO_3 and BF_4) obtained from CTA transformation and crystalline *c*-$[Au_2L_2](X)_2$ (X = CF_3SO_3 and BF_4) obtained from ATC transformation are given in Fig. S19 and Fig. 4 (see manuscript). Their emission characteristics and lifetimes are listed in Tables S2 and S3. The corresponding PXRD patterns are given in Fig. S20 and S21.

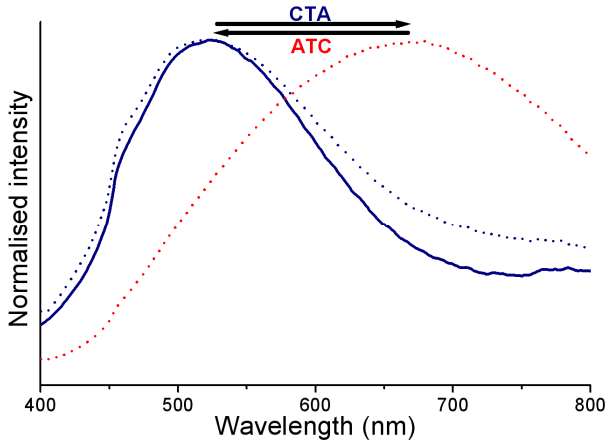

Fig. S19 Emission spectra of the crystalline *c*-$[Au_2L_2](CF_3SO_3)_2$ obtained from dichloromethane-assisted LAG (solid blue line), amorphous *a*-$[Au_2L_2](CF_3SO_3)_2$ obtained from CTA transformation (dotted red line) and crystalline *c*-$[Au_2L_2](CF_3SO_3)_2$ obtained from ATC transformation (dotted blue line).

Table S2 Emission, excitation characteristics and lifetimes of crystalline *c*-$[Au_2L_2](CF_3SO_3)_2$ obtained from dichloromethane-assisted LAG and *c*-$[Au_2L_2](CF_3SO_3)_2$ obtained from ATC transformation, as well as amorphous *a*-$[Au_2L_2](CF_3SO_3)_2$ obtained from CTA transformation and *a*-$[Au_2L_2](CF_3SO_3)_2$ obtained from water-assisted LAG.

Compound	λ_{em} (nm)	τ_1 (μs)	τ_2 (μs)
c-$[Au_2L_2](CF_3SO_3)_2$	460 sh, 525	2.5 (73%)	15 (27%)
c-$[Au_2L_2](CF_3SO_3)_2$ from ATC	463 sh, 521	2.4 (66%)	17 (34%)
a-$[Au_2L_2](CF_3SO_3)_2$ from CTA	670	3.8 (37%)	16 (63%)
a-$[Au_2L_2](CF_3SO_3)_2$	670	3.1 (34%)	14 (66%)

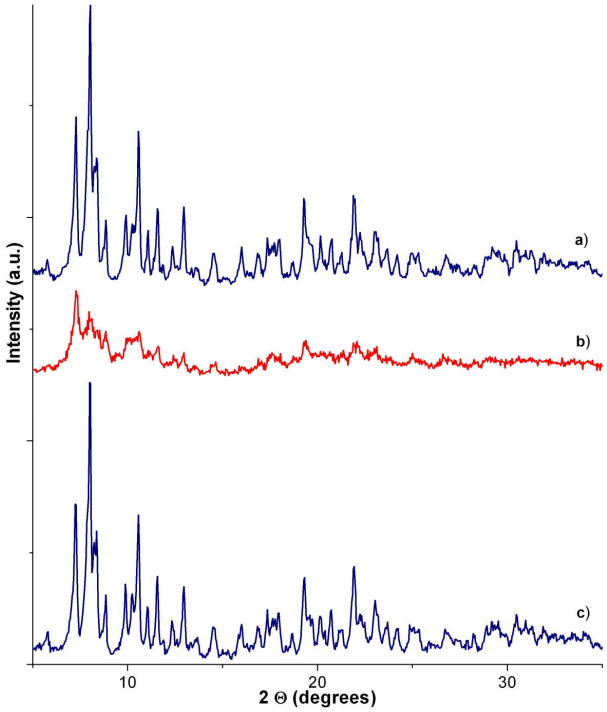

Fig. S20 PXRD patterns of a) crystalline *c*-$[Au_2L_2](CF_3SO_3)_2$ obtained from dichloromethane-assisted LAG (blue coloured), b) amorphous *a*-$[Au_2L_2](CF_3SO_3)_2$ obtained from CTA transformation (red coloured) and c) crystalline *c*-$[Au_2L_2](CF_3SO_3)_2$ obtained from ATC transformation (blue coloured).

Table S3 Emission, excitation characteristics and lifetimes of crystalline *c*-$[Au_2L_2](BF_4)_2$ obtained from dichloromethane-assisted LAG and *c*-$[Au_2L_2](BF_4)_2$ obtained from ATC transformation, as well as amorphous *a*-$[Au_2L_2](BF_4)_2$ obtained from CTA transformation and *a*-$[Au_2L_2](BF_4)_2$ obtained from water-assisted LAG.

Compound	λ_{em} (nm)	τ_1 (μs)	τ_2 (μs)
c-$[Au_2L_2](BF_4)_2$	447 sh, 457, 482 sh	3.8 (34%)	16 (66%)
c-$[Au_2L_2](BF_4)_2$ from ATC	445 sh, 457, 483 sh	3.7 (29%)	14 (71%)
a-$[Au_2L_2](BF_4)_2$ from CTA	692	3.9 (33%)	15 (67%)
a-$[Au_2L_2](BF_4)_2$	685	3.9 (35%)	14 (65%)

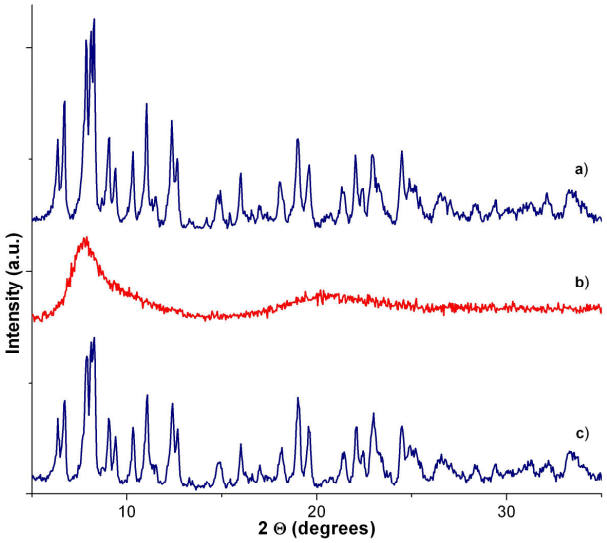

Fig. S21 PXRD patterns of a) crystalline *c*-$[Au_2L_2](BF_4)_2$ obtained from dichloromethane-assisted LAG (blue coloured), b) amorphous *a*-$[Au_2L_2](BF_4)_2$ obtained from CTA transformation (red coloured) and c) crystalline *c*-$[Au_2L_2](BF_4)_2$ compound obtained from ATC transformation (blue coloured).

$[Au_2L_2](X)_2$ (X = CF_3SO_3, SCN, BF_4 and PF_6) digold(I) helicates obtained from conventional solution-based anion-exchange

Further anion-exchange reactions were also performed in solution. Thus, NaX (X = CF_3SO_3, SCN, BF_4 and PF_6) salts (0.6 mmol) were suspended in a 20 mL dichloromethane solution of $[Au_2L_2](NO_3)_2$ (335 mg, 0.2 mmol). This mixture was stirred for 6 hours, shielded from light. The as-resulting suspension was filtered through Celite, and the solvent was removed under vacuum to give the anion-exchanged $[Au_2L_2](X)_2$ products as white powders. Yields: 312 mg (84.3%) for X = CF_3SO_3; 274 mg (82.2%) for X = SCN; 263 mg (76.2%) for X = BF_4 and 302 mg (82.0%) for X = PF_6.

Optical micrographs of anion-exchanged $[Au_2L_2](X)_2$ (X = CF_3SO_3, SCN, BF_4 and PF_6) helicates are shown in Figure S22. Photographs taken under hand held UV lamp (365 nm) illumination showing the solid-state emission colour of anion-exchanged $[Au_2L_2](X)_2$ (X = CF_3SO_3, SCN, BF_4 and PF_6) helicates are given in Figure S23. FT-IR, emission (λ_{ex} = 365 nm) and excitation spectra and the PXRD patterns of anion-exchanged $[Au_2L_2](X)_2$ complexes (X = CF_3SO_3, SCN, BF_4 and PF_6) are given in Fig. S24–S35. Emission, excitation characteristics and lifetimes are listed in Table S4.

The anion-exchange process was confirmed by the disappearance of strong band associated with nitrate anion at 1344 cm^{-1}, and appearance of characteristic bands associated with the exchanged-anions, such as triflate at 1259 and 1029 cm^{-1}, thiocyanate at 2107 cm^{-1}, tetrafluoroborate at 1048 cm^{-1} and hexafluorophosphate at 832 cm^{-1} in the IR spectra of the corresponding $[Au_2L_2](X)_2$ compounds. As revealed by PXRD, this process afforded one crystalline *c*-$[Au_2L_2](SCN)_2$ and three amorphous *a*-$[Au_2L_2](X)_2$ (X = CF_3SO_3, BF_4 and PF_6) digold(I) helicates.

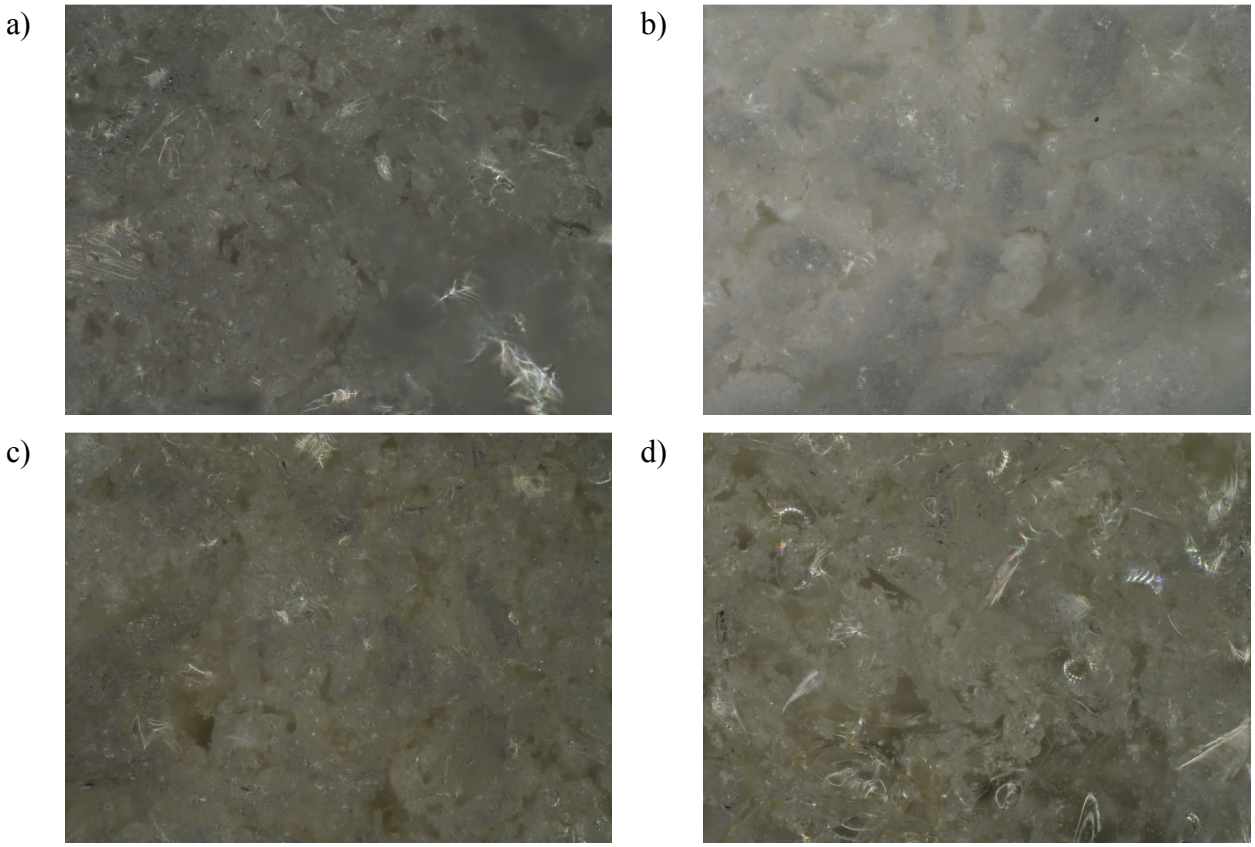

Fig. S22 Optical microscopic graphs of a) *a*-$[Au_2L_2](CF_3SO_3)_2$, b) *c*-$[Au_2L_2](SCN)_2$, c) *a*-$[Au_2L_2](BF_4)_2$ and d) *a*-$[Au_2L_2](PF_6)_2$ helicates obtained from conventional solution-based process.

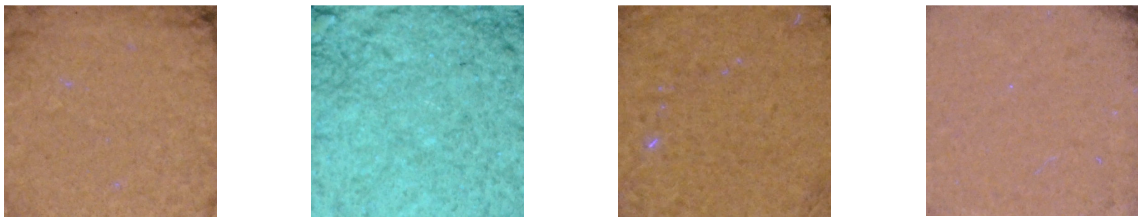

Fig. S23 Photographs taken under hand held UV lamp (365 nm) illumination showing the solid-state emission colour of a) *a*-$[Au_2L_2](CF_3SO_3)_2$, b) *c*-$[Au_2L_2](SCN)_2$, c) *a*-$[Au_2L_2](BF_4)_2$ and d) *a*-$[Au_2L_2](PF_6)_2$ helicates obtained from conventional solution-based process.

Amorphous *a*-$[Au_2L_2](CF_3SO_3)_2$ helicate obtained from conventional anion-exchange reaction

IR data: 3495 (b, w), 3064 (w), 2978 (w), 1609 (w), 1586 (w), 1481 (w), 1437 (m), 1403 (s), 1259 (s), 1221 (s), 1146 (s), 1097 (m), 1029 (s), 999 (m), 874 (w), 741 (m), 688 (m), 634 (m); Elemental analysis calcd. (%) for *a*-$[Au_2L_2](CF_3SO_3)_2$: C 51.96, H 3.49; found: C 51.65, H 3.74.

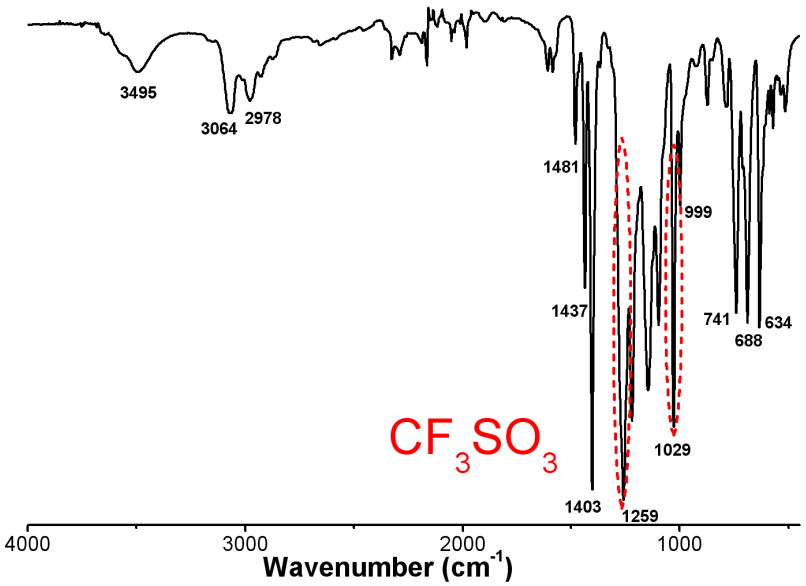

Fig. S24 FT-IR spectra of amorphous *a*-$[Au_2L_2](CF_3SO_3)_2$ complex obtained from conventional anion-exchange reaction.

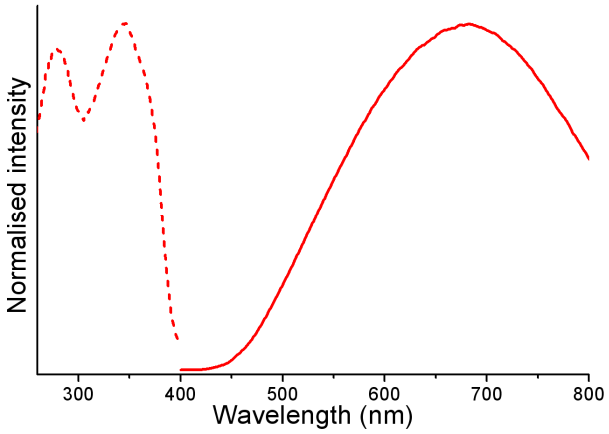

Fig. S25 Emission and excitation spectra of amorphous *a*-$[Au_2L_2](CF_3SO_3)_2$ helicate obtained from conventional anion-exchange reaction.

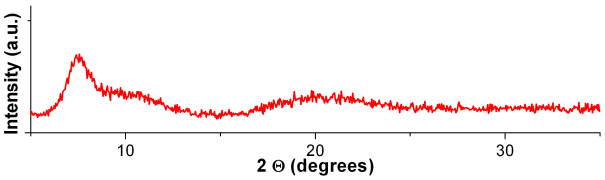

Fig. S26 PXRD patterns of amorphous *a*-$[Au_2L_2](CF_3SO_3)_2$ complex obtained from conventional anion-exchange reaction.

Crystalline *c*-[Au_2L_2]$(SCN)_2$ helicate obtained from conventional anion-exchange reaction

IR data: 3446 (vw), 3056 (w), 2975 (w), 2107 (s), 1480 (w), 1434 (m), 1404 (s), 1230 (m), 1097 (m), 999 (w), 737 (m), 688 (m); Elemental analysis calcd. (%) for *c*-[Au_2L_2]$(SCN)_2$: C 57.63, H 3.87, N 1.68; found: C 57.46, H 3.88, N 1.41.

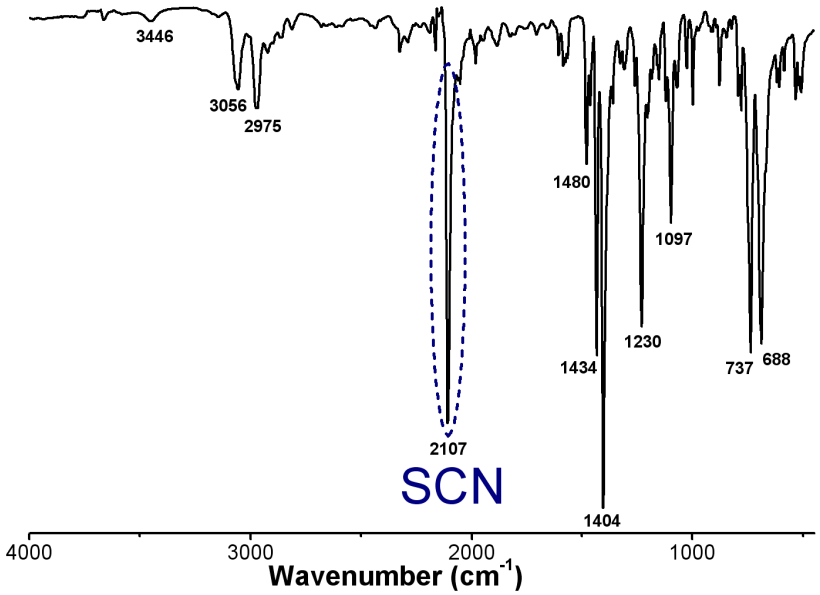

Fig. S27 FT-IR spectra of crystalline *c*-[Au_2L_2]$(SCN)_2$ complex obtained from conventional anion-exchange reaction.

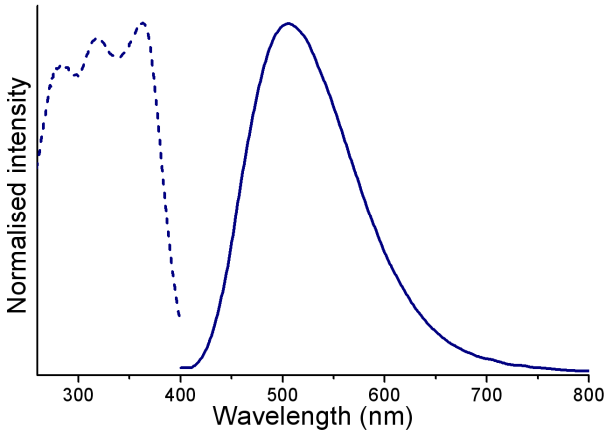

Fig. S28 Emission and excitation spectra of crystalline *c*-[Au_2L_2]$(SCN)_2$ helicate obtained from conventional anion-exchange reaction.

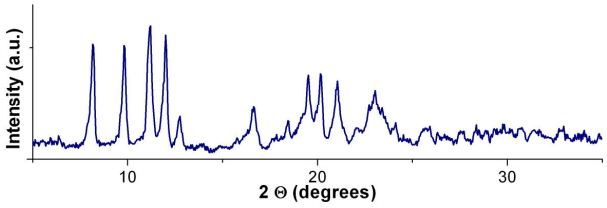

Fig. S29 PXRD patterns of crystalline *c*-[Au_2L_2]$(SCN)_2$ complex obtained from conventional anion-exchange reaction.

Amorphous *a*-$[Au_2L_2](BF_4)_2$ helicate obtained from conventional anion-exchange reaction

IR data: 3634 (w), 3064 (w), 2976 (w), 2165 (w), 1609 (w), 1586 (w), 1481 (w), 1437 (m), 1402 (s), 1220 (m), 1048 (s), 997 (m), 873 (w), 741 (m), 688 (m); Elemental analysis calcd. (%) for *a*-$[Au_2L_2](BF_4)_2$: C 54.32, H 3.74; found: C 54.27, H 4.00.

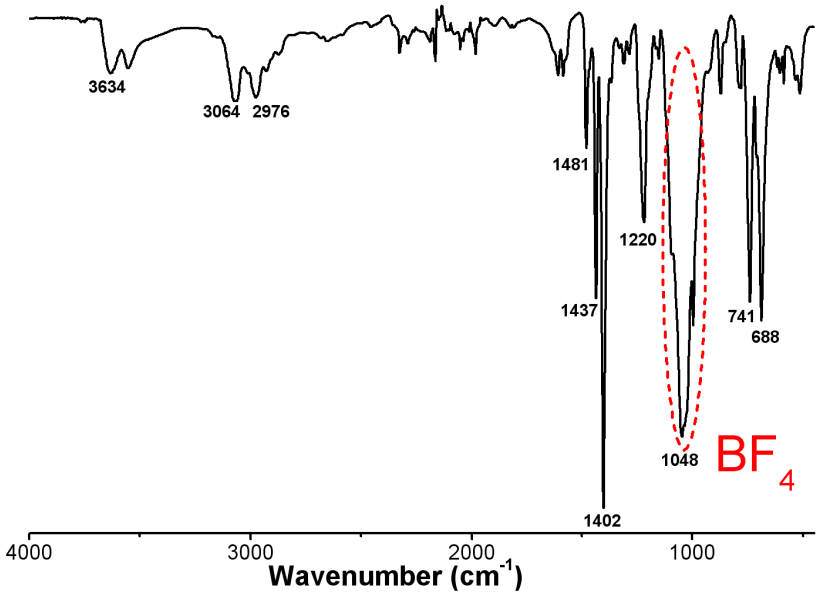

Fig. S30 FT-IR spectra of amorphous *a*-$[Au_2L_2](BF_4)_2$ complex obtained from conventional anion-exchange reaction.

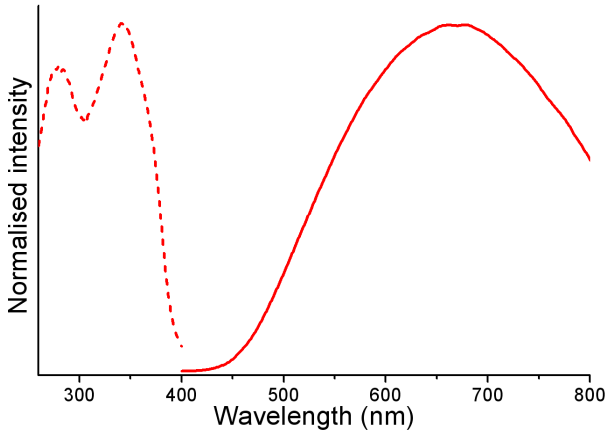

Fig. S31 Emission and excitation spectra of amorphous *a*-$[Au_2L_2](BF_4)_2$ helicate obtained from conventional anion-exchange reaction.

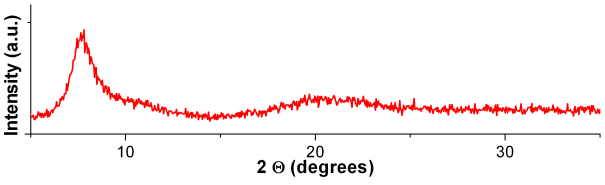

Fig. S32 PXRD patterns of amorphous *a*-$[Au_2L_2](BF_4)_2$ complex obtained from conventional anion-exchange reaction.

Amorphous *a*-$[Au_2L_2](PF_6)_2$ helicate obtained from conventional anion-exchange reaction

IR data: 3076 (w), 2977 (w), 2325 (w), 1635 (w), 1606 (w), 1587 (w), 1481 (w), 1437 (m), 1402 (s), 1219 (m), 1098 (m), 999 (w), 832 (s), 786 (m), 741 (m), 688 (m), 556 (m); Elemental analysis calcd. (%) for *a*-$[Au_2L_2](PF_6)_2$: C 50.88, H 3.50; found: C 50.60, H 3.78.

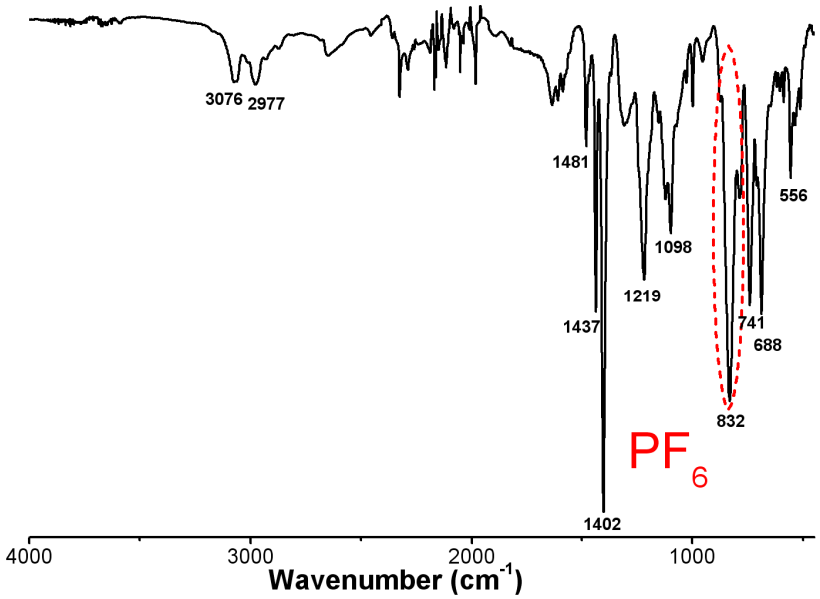

Fig. S33 FT-IR spectra of amorphous *a*-$[Au_2L_2](PF_6)_2$ complex obtained from conventional anion-exchange reaction.

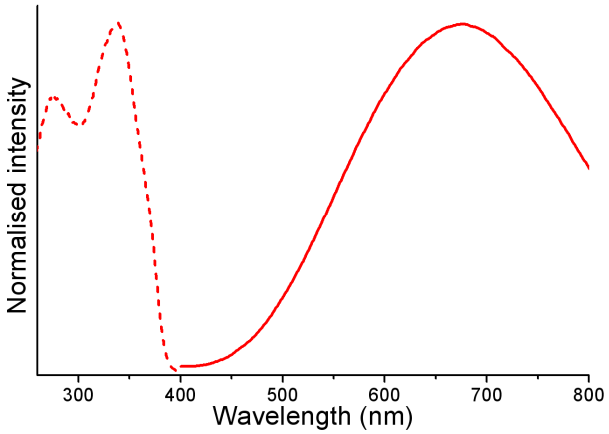

Fig. S34 Emission and excitation spectra of amorphous *a*-$[Au_2L_2](PF_6)_2$ helicate obtained from conventional anion-exchange reaction.

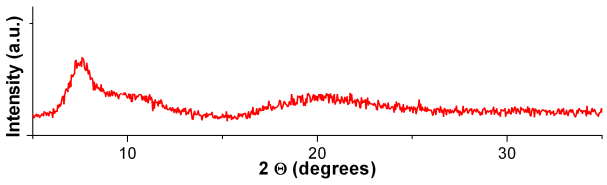

Fig. S35 PXRD patterns of amorphous *a*-$[Au_2L_2](PF_6)_2$ complex obtained from conventional anion-exchange reaction.

Table S4 Emission, excitation characteristics and lifetimes of crystalline *c*-$[Au_2L_2](X)_2$ (X = SCN) and amorphous *a*-$[Au_2L_2](X)_2$ (X = CF_3SO_3, BF_4 and PF_6) helicates obtained from conventional solution-based anion-exchange reaction.

Compound	λ_{em} (nm)	λ_{ex} (nm)	τ_1 (μs)	τ_2 (μs)
a-$[Au_2L_2](CF_3SO_3)_2$	683	280, 344	3.0 (36%)	13 (64%)
c-$[Au_2L_2](SCN)_2$	506	284, 318, 362	0.4 (63%)	5.4 (37%)
a-$[Au_2L_2](BF_4)_2$	672	280, 341	2.9 (33%)	13 (67%)
a-$[Au_2L_2](PF_6)_2$	678	275, 339	3.6 (34%)	15 (66%)

Acknowledgement

We thank the assistance provided by Dr. Judith Mihály for recording the FT-IR spectra, Márta Roczkov for EA measurements, István Sajó for recording the PXRD spectra. We gratefully acknowledge the assistance provided by Attila Stamm (Auro-Science Consulting Kft., Budapest, Hungary) in the collection of optical micrographs.

References

1 A. Deák, T. Megyes, G. Tárkányi, P. Király, L. Biczók, G. Pálinkás, P. J. Stang, *J. Am. Chem. Soc.,* 2006, **128**, 12668.